CEAS Space Journal (2021) 13:51–64
https://doi.org/10.1007/s12567-020-00319-3

ORIGINAL PAPER

Stability analysis and flight control design of the winged reusable launch vehicle ReFEx

Daniel Kiehn[1]

Received: 9 January 2020 / Revised: 4 May 2020 / Accepted: 28 May 2020 / Published online: 30 June 2020

Abstract

The German Aerospace Center (DLR) is currently studying different technologies for reusable launch vehicles (RLVs) to evaluate and compare their benefits. The project CALLISTO (Cooperative Action Leading to Launcher Innovation in Stage Toss-back Operations) investigates a VTVL (vertical takeoff, vertical landing) concept. In the DLR project ReFEx (reusability flight experiment), in the context of which this paper is presented, a winged VTHL (vertical takeoff, horizontal landing) concept is investigated to develop the key technologies for future winged RLV applications, culminating in a flight experiment to demonstrate the capability of controlled autonomous return flight from supersonic to subsonic speeds. In this paper, analysis of stability and controllability is used on a three-dimensional envelope of points to derive a suitable flight corridor for the re-entry. Second, a controller concept based on inversion of the rotational equations of motion is derived. The validity of the presented controller concept is shown on a preliminary level via comparison of open-loop and closed-loop dynamics at two representative flight points and a time simulation which includes a segment of the planned mission.

Keywords ReFEx · Reusable launch vehicle · Stability analysis · Flight control design

Abbreviations

CALLISTO	Cooperative Action Leading to Launcher Innovation in Stage Toss-back Operations
CNES	Centre National d'Études Spatiales (French Aerospace Centre)
DLR	Deutsches Zentrum für Luft- und Raumfahrt (German Aerospace Center)
DoF	Degree(s) of freedom
FCS	Flight control system
GNC	Guidance, navigation and control
HNS	Hybrid navigation system
ISA	International standard atmosphere
JAXA	Japan Aerospace Exploration Agency
LFBB	Liquid flyback booster
NDI	Nonlinear dynamic inversion
RCS	Reaction control system
ReFEx	Reusability Flight Experiment
RLV	Reusable launch vehicle
SHEFEX	Sharp Edge Flight Experiment
VTHL	Vertical takeoff, horizontal landing
VTVL	Vertical takeoff, vertical landing
WGS84	World Geodetic System 1984

Symbols

A	System matrix
$C_{l,m,n}$	Rolling, pitching and yawing moment coefficients
D	Damping ratio
I	Inertia matrix
L, M, N	Rolling, pitching and yawing moment in body axes
l_μ	Reference length
Ma	Mach number
p, q, r	Roll, pitch and yaw rate
$\bar{q}$	Dynamic pressure
V	Airspeed
t_{DA}	Time to double amplitude
t_{HA}	Time to half amplitude
α	Angle of attack
β	Angle of sideslip
γ	Flight path angle
ζ	Rudder deflection
η_L, η_R	Left and right canard deflections
λ	Eigenvalue
μ_a	Air-path bank angle

✉ Daniel Kiehn
daniel.kiehn@dlr.de

[1] German Aerospace Center (DLR), Institute of Flight Systems, Lilienthalplatz 7, 38108 Brunswick, Germany

Φ, Θ, Ψ	Euler angles of roll, pitch, yaw
χ	Azimuth angle

Indices and Subscripts

a	Aerodynamic axes
b	Body axes
c	Command
K	Inertial quantity

1 Introduction

The German Aerospace Center (DLR) is currently studying different technologies for reusable launch vehicles (RLVs) to evaluate and compare their benefits [1, 2]. The project CALLISTO (Cooperative Action Leading to Launcher Innovation in Stage Toss-back Operations)[1] investigates a VTVL (vertical takeoff, vertical landing) concept [3, 4]. In the DLR project ReFEx (Reusability Flight Experiment), which is the focus of this paper, a winged VTHL (vertical takeoff, horizontal landing) concept is investigated to develop the key technologies for future RLV applications, with the final objective of demonstrating controlled autonomous re-entry of a winged vehicle from hypersonic velocities down to the subsonic range. An overview of the project and its goals can be found in [5, 6].

The ReFEx re-entry vehicle is a sub-scale demonstrator and has an expected mass of about 400 kg, is approximately 2.7 m in length and has a wingspan of about 1.1 m. The wide Mach number range the vehicle experiences during its mission imposes challenging requirements on its aerodynamic design and the guidance, navigation, and control (GNC) subsystems, including the flight control system (FCS). Finding a suitable aerodynamic configuration for the demonstrator and designing its GNC system are hence core tasks of the project [7].

To a certain degree, ReFEx is the successor of DLR's most recent re-entry experiment, the Sharp Edge Flight Experiment SHEFEX II, which was launched from the Andøya rocket range in Norway in June 2012 [8]. It had a faceted axially symmetric shape with four canards and was fitted with an FCS for attitude control, but did not have a guidance system. Due to the absence of significant lifting surfaces, its trajectory was almost purely ballistic. The FCS implemented for SHEFEX II was an inversion-based attitude controller with fixed allocation of the control surfaces (refer to [9] for details about the control design). ReFEx on the other hand will be equipped with a full GNC system, which requires the integration of the outer guidance loops with the inner attitude controller. The lifting surfaces of ReFEx also mean that the impact of aerodynamic forces on the flight path will be much more significant than they were in case of SHEFEX II, which requires a more sophisticated controller design.

In the recent past, nonlinear dynamic inversion (NDI) has been used in flight control design for re-entry vehicles or supermaneuverable aircraft; see for example [10–12] and the references therein. The flight control architecture presented in this paper is partially based on [10, 12], but also takes into account the effects of the first and second derivatives of the flight path angle γ and the azimuth angle χ in the inversion of the rotational equations of motion.

In this paper, stability and controllability analysis of the ReFEx vehicle is utilized to derive a suitable flight corridor for re-entry. Then, an inversion-attitude controller concept is presented and its suitability to the considered problem is shown on a preliminary level via comparison of open-loop and closed-loop dynamics in two different flight conditions. Finally, the controller is put to test in a time simulation of a critical segment of the mission.

2 Mission and vehicle

ReFEx is foreseen to be launched by a Brazilian solid-fuel two-stage VSB-30 sounding rocket from a range near the Woomera test area, Australia [13]. After departing from the guiding rail, the rocket ascends unguided with passive spin stabilization using four fins on each stage. Spin stabilization of the rocket also reduces dispersion at payload separation and stage impact. A hammerhead fairing of 0.64 m diameter covers the tail section and the wings, which are folded during ascent as shown in Fig. 1a to fulfill the stability requirements of the rocket [13, 14]. The fairing also incorporates a dummy fin which is needed to maintain some level of aerodynamic symmetry during the ascent. An overview of the mission is shown in Fig. 2, and a more detailed information on the mission can be found in [6]. After the burn-out of the second stage a yo–yo de-spin system is used to reduce the rotational rate of the vehicle to a minimum, followed by the separation of the fairing and unfolding of the wings.

The ReFEx vehicle, which is now in re-entry configuration as shown in Fig. 1b, is to perform a re-entry which is representative for that of full-scale winged reusable stages. Based on former research of winged RLV concepts such as the Liquid Fly-Back Booster (LFBB) and the EVEREST (Evolved European Reusable Space Transport), a re-entry corridor was defined which describes a Mach number-altitude corridor representative for winged RLVs [15]. Achieving a re-entry trajectory within the boundaries of this RLV corridor is the primary goal of the flight experiment. After de-spin, while still in the outer atmosphere where the density is low, the vehicle's attitude is controlled by the FCS using a

[1] An international cooperation between DLR, CNES (Centre National d'Études Spatiales: French Aerospace Centre) and JAXA (Japan Aerospace Exploration Agency).

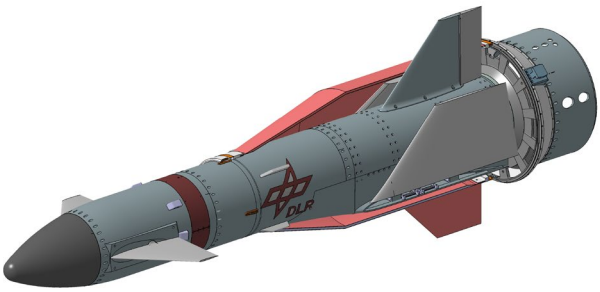

(a) ReFEx launch segment, fairing and dummy fin in red

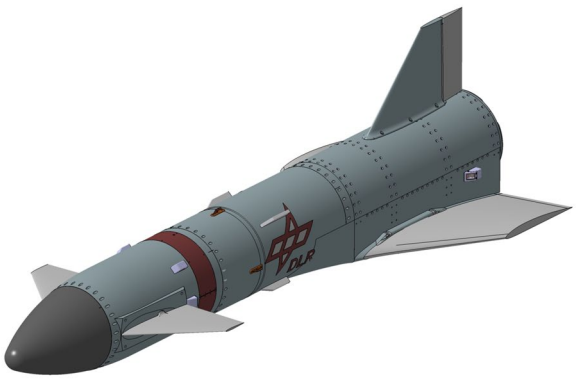

(b) ReFEx re-entry vehicle

Fig. 1 ReFEx launch and re-entry segments

nitrogen-based cold gas reaction control system (RCS) consisting of eight thruster nozzles located at the aft of the vehicle. ReFEx is to maintain an inverted attitude with the fin pointing downward (for reasons explained in Sect. 3) until it reaches the entry interface [5], where the dynamic pressure first reaches the threshold of 5 kPa (the projected altitude for this point is approximately 60 km). The aerodynamic control surfaces (left and right canards, rudder) are enabled at this point, while the RCS is still used in parallel for some time to maintain maximum control authority. After this short phase of hybrid control, the RCS will not be activated by the FCS anymore and all control is transferred to the aerodynamic control surfaces: two canards which mainly produce pitching and rolling moments, and the rudder which primarily provides yawing moments. The control effectiveness of all aerodynamic surfaces however is extremely dependent on the flight condition (especially the angle of attack α) and the cross-coupling effects (such as the rolling moment due to rudder deflection) are very significant, so the actual control surface allocation to produce the desired rolling, pitching and yawing moments is performed dynamically by the flight controller as described in Sect. 4.

At approximately Mach 2, a transition maneuver will be performed to change from inverted to regular flight attitude (refer to Sect. 3 for details), in which ReFEx will continue decelerating down to the ground.

3 Open-loop stability analysis

A major goal of the ReFEx project is to find a vehicle configuration which is aerodynamically stable throughout the whole mission [7]. After multiple design iterations in which the geometry of the vehicle was changed significantly, a somewhat promising configuration was found. The flight mechanical analysis of this configuration, however, revealed severe instabilities of the lateral motion in certain flight regimes (for a description of the last design stages, see [14]), which made clear that the trajectory that was originally foreseen could not be achieved with the flight control hardware and software available in the project and without changing the aerodynamic shape of the vehicle radically. It was then investigated if a feasible solution could be found without changing the vehicle significantly, but by conducting the re-entry flight in different attitudes at different speeds and thereby exploiting the fact that the aerodynamic characteristics of the vehicle change considerably with the Mach number and the angle of attack. The feasibility of this option was explored using a bottom-up approach: first, the absolute necessity of the requirement of natural stability in all flight conditions was reconsidered. Eventually, the requirement was relaxed [16] because it could only have been achieved via another costly configuration change. In the second step, which aimed to find a suitable flight envelope, a large set of discrete points was defined by varying the Mach number, the angle of attack α and the altitude H, resulting in a three-dimensional array of discrete points $(\mathrm{Ma}_j, \alpha_j, H_j)$ with an equidistant grid, as described by Eqs. (1)–(3).

$$\mathrm{Ma}_j \in \{0.4, 0.6, \ \ldots\ , \ 5.0\}, \tag{1}$$

$$\alpha_j \in \{-50°, -49°, \ \ldots\ , \ 20°\}, \tag{2}$$

$$H_j \in \{2\ \mathrm{km}, 4\ \mathrm{km}, \ \ldots\ , \ 20\ \mathrm{km}\}. \tag{3}$$

The chosen range of values for the angle of attack covers the maximum (positive and negative) angles of attack which were deemed feasible for the experiment by mission analysis. The upper Mach number boundary corresponds to the maximum Mach number the vehicle is expected to experience during the mission, while the lower boundary is well below the Mach number region which is most critical in terms of stability and controllability (approx. Mach 0.8). The altitude range was chosen low (≤ 20 km) because it proved to be most critical in terms of stability.

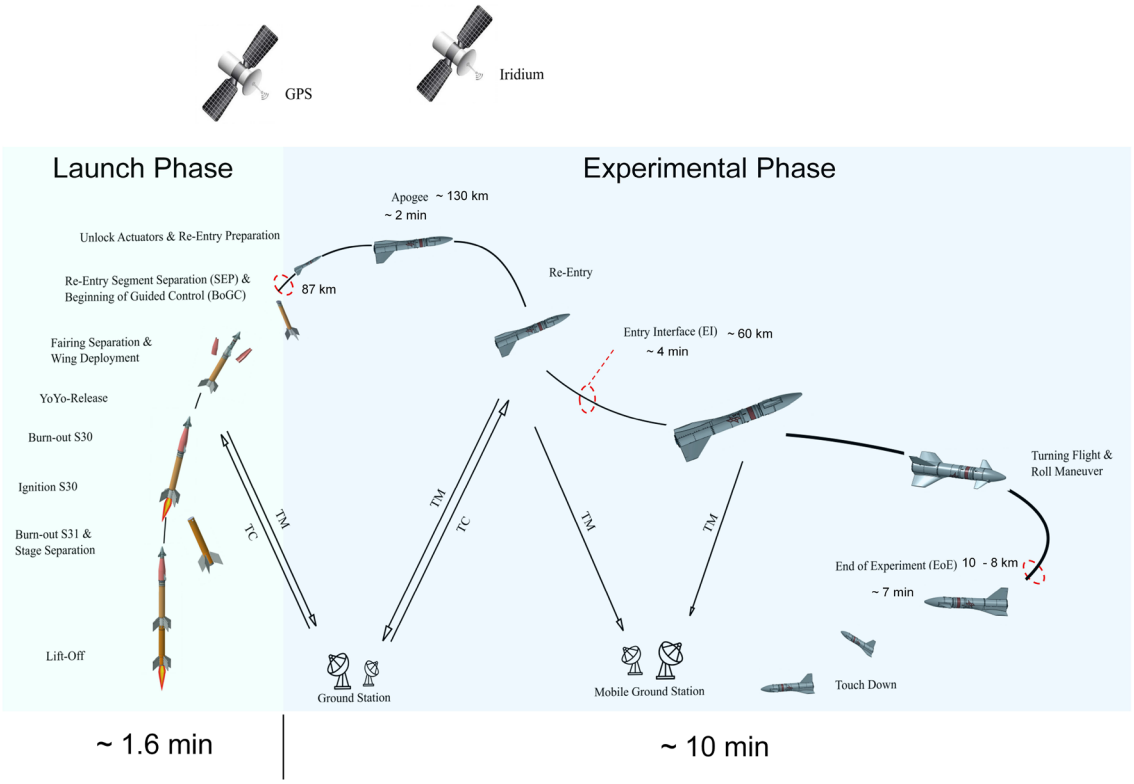

Fig. 2 Overview of the ReFEx mission [6]

The coordinate frame definition used for ReFEx follows the standards of ISO 1151/1, but due to the rather unusual flight path planned for the mission, some clarification is presented here: a negative angle of attack means that the vertical fin is on the windward side of the vehicle, i.e., it is directly exposed to the airflow. A negative angle of attack usually means negative lift, but during most of the flight experiment some lift acting against the gravitational force is required. Thus, during the flight experiment, negative angles of attack will usually correspond to an inverted flight state, where the vertical fin is oriented toward Earth. To avoid ambiguities, the following definitions will be used for the remainder of this paper: *regular* flight attitude corresponds to a positive angle of attack ($\alpha \geq 0°$), with the fin oriented away from Earth, i.e., $\boldsymbol{\Phi} = \mu = 0°$. On the contrary, *inverted* flight attitude denotes a negative angle of attack ($\alpha < 0°$) where the vertical fin is oriented toward the Earth (i.e., $\boldsymbol{\Phi} = \mu = 180°$). These definitions, which are visualized in Fig. 3, are to be understood as reference cases for stability analysis: during the mission the commanded aerodynamic bank angle μ_c will not be limited to 0° or 180° — in fact, the guidance system uses μ as the main control variable (refer to [17] for details about the guidance algorithms).

At each point (triplet of Mach number, α, and altitude), the vehicle is trimmed for an equilibrium of rotational accelerations ($\dot{p} = \dot{q} = \dot{r} = 0$) to obtain the required deflections of the left and right canard (η_L and η_R) and the rudder deflection ζ. Since ReFEx has no engines and no redundant control surfaces, control is limited to the three rotational degrees of freedom (3DoF), and translational accelerations are accepted as a consequence. After trimming, well-established methods can be used for stability analysis of the open-loop system: numerical linearization around a resulting trim point yields the corresponding system matrix A for that flight condition, and the complex eigenvalues of A describe the system dynamics.

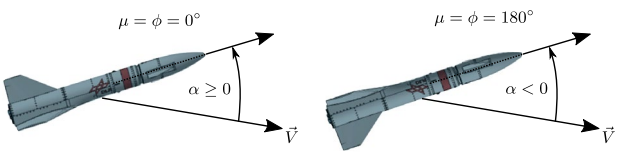

(a) Regular attitude **(b)** Inverted attitude

Fig. 3 Reference cases for stability analysis

Table 1 Stability categories based on the maximum real part

Re_{max} in rad/s	Category	Flight point accepted	Color in Fig. 4
$Re_{max} \leq 0$	Natural or neutral stability	Yes	Green
$0 < Re_{max} \leq 0.05$	Minor instability	Yes	Yellow
$0.05 < Re_{max} \leq 0.1$	Major instability	Yes	Orange
$Re_{max} > 0.1$	Critical instability	No	Red
N/A	Insufficient control authority	No	Gray

The flight dynamics model used for linearization contains rigid-body dynamics, and the effects of flexibility are not considered. It is assumed that these effects will play a minor role in the real mission due to the compact and rigid structure of the vehicle. Actuator dynamics such as backlash or delays were neglected (apart from deflection limits). Additionally, only the first-order terms of the Taylor approximations are considered in the numerical linearization. The impact of the neglected flexibility effects, actuator dynamics, and higher-order terms of the Taylor series, e.g. from rapidly changing atmospheric conditions, will be subject to future work.

Each eigenvalue λ_i of A yields the characteristic (second-order equivalent) angular frequency ω_i and the damping ratio D_i of the corresponding mode via Eqs. (4) and (5), respectively [18].

$$\omega_i = \|\lambda_i\| = \sqrt{\mathrm{Re}(\lambda_i)^2 + \mathrm{Im}(\lambda_i)^2}, \tag{4}$$

$$D_i = -\frac{\mathrm{Re}(\lambda_i)}{\omega_i}. \tag{5}$$

The time to half amplitude of a characteristic mode relates to the real part of its corresponding eigenvalue λ_i via [18]:

$$t_{\mathrm{HA}} = -\frac{\ln(2)}{\mathrm{Re}(\lambda_i)}. \tag{6}$$

If the motion is unstable, indicated by a positive real part of the eigenvalue, t_{HA} becomes negative and $t_{\mathrm{DA}} = -t_{\mathrm{HA}}$ can be interpreted as the time to double amplitude. The least stable motion in a certain flight condition can therefore be captured by evaluating the highest occurring real part of all eigenvalues. To evaluate the stability of a flight point with only one criterion, the highest occurring real part Re_{max} of the system was considered, regardless of the corresponding mode:

$$Re_{max} = \max_i \left(\mathrm{Re}(\lambda_i)\right). \tag{7}$$

Since the system matrix A in the considered case includes the longitudinal and lateral dynamics, there is no distinction of the source of the most critical eigenvalue (longitudinal or lateral motion) which constitutes the maximum real part Re_{max}. This approach is conservative as it applies the same strict criteria for longitudinal and lateral dynamics, even though the control authority around the different axes is generally different and strongly dependent on the flight condition (the Mach number and the angle of attack).

For each flight point, the eigenvalues are analyzed and the point is assigned a stability category based on the highest real part Re_{max} according to Table 1. At this early stage of vehicle design and development of the flight controller, neither the hardware to be used in the project was known, nor the atmospheric disturbances to be expected during the mission and the measurement accuracies of the navigation message provided by the hybrid navigation system (HNS) and the connected sensors. Hence, the threshold for admissible maximum real parts had to be chosen quite conservatively and based on experience. For the maximum admissible real part Re_{max}, a threshold of 0.1 rad/s was chosen. It is expected that the actual GNC system and connected subsystems will be capable of dealing with significantly higher real parts, but a conservative threshold results in higher requirements on the flight controller and a more restrictive flight envelope.

The results of the aforementioned analysis are visualized in Fig. 4. Flight conditions (combinations of Mach number, angle of attack, and altitude) where a trim (moment equilibrium) cannot be achieved or pitch control authority $C_{m\eta}$ is insufficient are marked in gray. The stability of a flight point is marked in a color other than gray only if a trim can be achieved and control authority is sufficient; the color represents the range of the maximum real part where green represents natural or at least neutral stability, red means insufficient stability, and yellow and orange represent intermediate ranges (the thresholds are given in Table 1).

It is apparent that the vehicle is insufficiently stable in the region of Mach 3 to Mach 5 and angles of attack α higher than approx. $-10°$. The cause for this is that the longitudinal motion is statically unstable here ($C_{m\alpha} > 0$), but also the lateral motion is unstable for higher angles of attack (approx. $\alpha > 10°$) because the vertical fin is in the wake of the vehicle under these conditions and thereby loses its effectiveness, which eventually causes a lack of directional stability. As

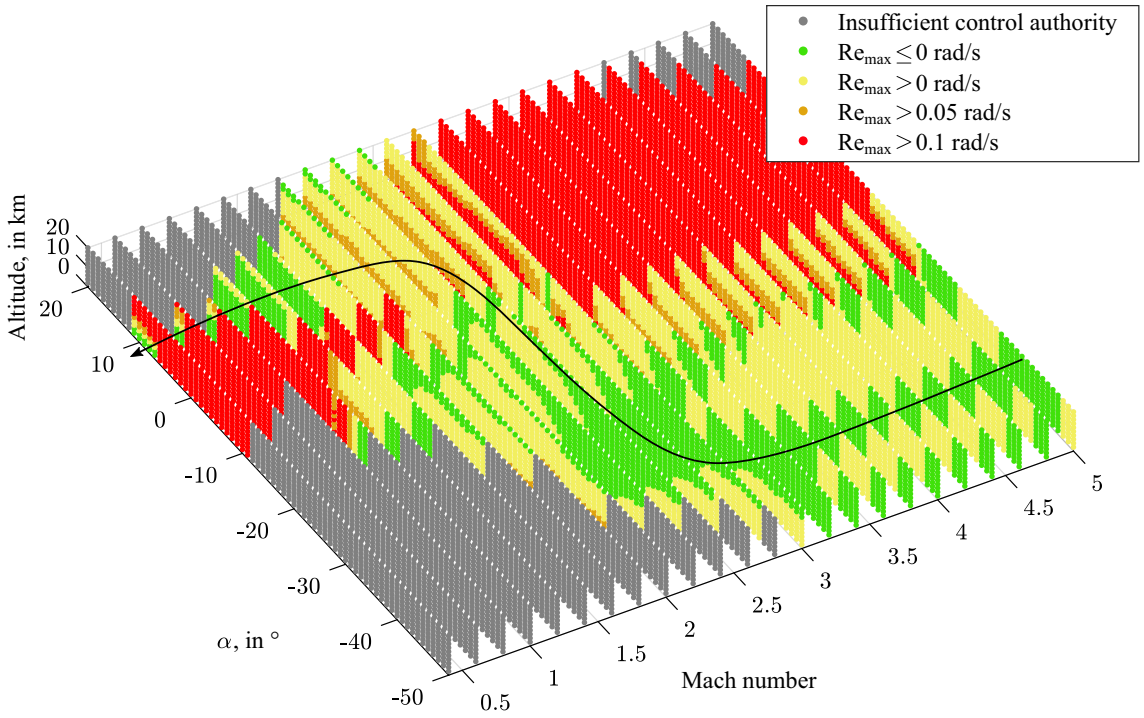

Fig. 4 Three-dimensional stability envelope (black: exemplary flight path)

a consequence, the region of higher Mach numbers will have to be flown inverted. In lower Mach number regimes, however, the vehicle is not trimmable in inverted flight attitude anymore, causing the need for a transition maneuver to change from inverted to regular attitude. This maneuver could be used to rotate the vehicle, e.g., from $\Phi = 180°$ and $\alpha = -20°$ to a regular attitude with $\Phi = 0°$ and $\alpha = 10°$ at a speed of Mach 2.

To achieve the desired change in the aerodynamic bank angle μ, a roll around the aerodynamic velocity vector is required, which in turn requires a coordinated rotation around all three body-fixed axes (two, if $\beta = 0$). The desired additional change of the angle of attack is obtained via a rotation around the body-fixed y-axis y_b. The aforementioned transition maneuver hence requires coordination of rotational accelerations and rates around all three body axes, even in the case of $\beta = 0$. This is visualized in Fig. 5, where the relationship between the relevant coordinate frames is shown.

The flight controller has to coordinate the angular accelerations and rates during this transition maneuver to ensure that the aerodynamic bank angle μ and the angle of attack α follow their desired profiles, while the sideslip angle remains near zero.

After the transition maneuver ReFEx continues decelerating in regular attitude. Note that the corridor of angles of attack where the vehicle is sufficiently stable and

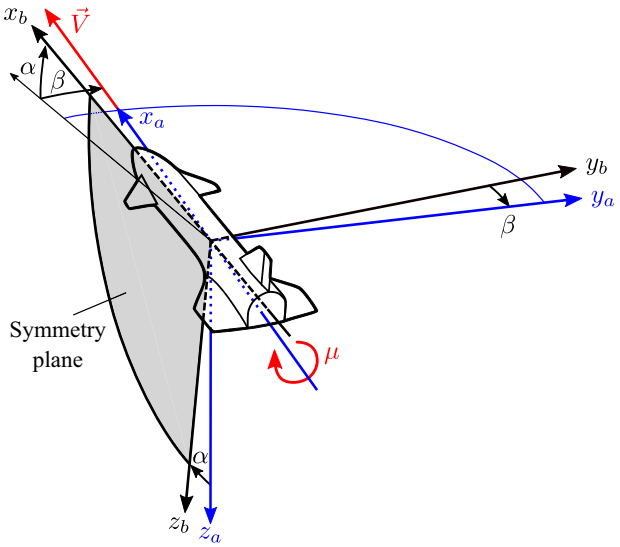

Fig. 5 Rotation around the velocity vector $\vec{V}$

controllable is very narrow for Mach < 1 , which poses high requirements on the GNC system as a whole. Recalling however that the value of 0.1 rad/s defined for $\mathrm{Re}_{\max}$ is expected to be overcautious, the actual flyable Ma-α-altitude corridor is expected to turn out larger than the narrow region visible in Fig. 4. Regardless of the controller performance, it is still beneficial to stay in more stable regions, because improved

stability reduces the required control activity and hence reduces dynamic actuator loads.

4 Controller design

The flight control system can mainly be divided into two subsystems: first, the guidance system, which forms the outer loop. Its task is to generate and adapt a target trajectory for the vehicle to follow, based on the current flight point. More details on the preliminary design of the guidance algorithms for ReFEx, which are primarily energy-based, can be found in [17] and [19].

The inner loop, designated in this paper as the *flight controller*, has to stabilize the vehicle and ensure that it follows the commands given by the guidance while rejecting any external disturbances. The guidance commands in the presented case are the desired aerodynamic bank angle μ_c, the angle of attack α_c and the sideslip angle β_c, as well as their corresponding first and second derivatives $(\dot{\mu}, \dot{\alpha}, \dot{\beta})_c^T$ and $(\ddot{\mu}, \ddot{\alpha}, \ddot{\beta})_c^T$, respectively. Using the derivatives as additional inputs to the flight controller enables a smoother processing of the commands, because potential upcoming changes of the commands are already known up to their second derivative at the current time.

To obtain the rotational accelerations $(\dot{p}, \dot{q}, \dot{r})_c^T$ required to follow the commands of the guidance, the relationship between the derivatives of the kinematic bank angle μ_K, the kinematic angle of attack α_K and the kinematic sideslip angle β_K to the body-fixed rotational rates $(p, q, r)^T$ and the respective derivatives of the flight path angle γ as well as the azimuth angle χ, which is expressed in Eq. (8) [20], can be used as a starting point.

$$\begin{pmatrix} \dot{\mu}_K \\ \dot{\alpha}_K \\ \dot{\beta}_K \end{pmatrix} = \underbrace{\begin{pmatrix} \frac{\cos\alpha_K}{\cos\beta_K} & 0 & \frac{\sin\alpha_K}{\cos\beta_K} \\ -\cos\alpha_K \tan\beta_K & 1 & -\sin\alpha_K \tan\beta_K \\ \sin\alpha_K & 0 & -\cos\alpha_K \end{pmatrix}}_{T_1} \begin{pmatrix} p \\ q \\ r \end{pmatrix} + \underbrace{\begin{pmatrix} \cos\mu_K \tan\beta_K & \sin\gamma + \sin\mu \tan\beta_K \cos\gamma \\ -\frac{\cos\mu_K}{\cos\beta_K} & -\frac{\sin\mu_K \cos\gamma}{\cos\beta_K} \\ -\sin\mu_K & \cos\mu_K \cos\gamma \end{pmatrix}}_{T_2} \begin{pmatrix} \dot{\gamma} \\ \dot{\chi} \end{pmatrix}. \tag{8}$$

Note that Eq. (8) is invalid if $\beta_K = \pm\frac{\pi}{2}$, but it can be safely assumed that this off-nominal condition will not be met during the mission, and also it can be treated explicitly.

Equation (8) describes a kinematic relationship which also holds in the presence of wind. To simplify the notation for this paper, the absence of wind is assumed, in which case the inertial axes (indicated by the index K) coincide with the aerodynamic axes denoted by the index a, and the notation can be simplified via Eqs. (9)– (13).

$$\mu_K = \mu_a = \mu, \tag{9}$$

$$\alpha_K = \alpha_a = \alpha, \tag{10}$$

$$\beta_K = \beta_a = \beta, \tag{11}$$

$$\gamma_a = \gamma, \tag{12}$$

$$\chi_a = \chi. \tag{13}$$

Using this assumption and the corresponding notation, which will be applied in the remainder of this paper, the rotational accelerations $(\dot{p}, \dot{q}, \dot{r})_c^T$ required to track the guidance commands can be obtained by differentiating Eq. (8) with respect to the time, as described in Eq. (14).

$$\begin{pmatrix} \dot{p} \\ \dot{q} \\ \dot{r} \end{pmatrix}_c = {T_1}^{-1} \left[\begin{pmatrix} \ddot{\mu} \\ \ddot{\alpha} \\ \ddot{\beta} \end{pmatrix}_c - \dot{T}_1 \begin{pmatrix} p \\ q \\ r \end{pmatrix} - \dot{T}_2 \begin{pmatrix} \dot{\gamma} \\ \dot{\chi} \end{pmatrix} - T_2 \begin{pmatrix} \ddot{\gamma} \\ \ddot{\chi} \end{pmatrix} \right]. \tag{14}$$

The rotational accelerations resulting from Eq. (14) yield the required moments and corresponding moment coefficients by inverting the rotational equations of motion, as expressed by Eq. (15).

$$\begin{pmatrix} C_l \\ C_m \\ C_n \end{pmatrix}_c = \frac{1}{\bar{q} S l_\mu} \begin{pmatrix} L \\ M \\ N \end{pmatrix} = \frac{1}{\bar{q} S l_\mu} \left[I \begin{pmatrix} \dot{p} \\ \dot{q} \\ \dot{r} \end{pmatrix}_c + \begin{pmatrix} p \\ q \\ r \end{pmatrix} \times I \begin{pmatrix} p \\ q \\ r \end{pmatrix} \right]. \tag{15}$$

The control surface deflections of the canards and rudder $(\eta_L, \eta_R, \zeta)^T$ required to achieve the commanded moment coefficients $(C_l, C_m, C_n)_c^T$ are obtained via inversion of the aerodynamic model. In practice, this inversion will require measurements and estimations which are potentially faulty and noisy. In this paper, the availability of perfect measurements and a perfect aerodynamic database is assumed to obtain a proof of concept for the presented controller architecture. To fully prove the validity of the presented controller, the effects of these inaccuracies will have to be investigated. Since there are three moments to be produced by three independent control surfaces, the solution of this model inversion is unique for any set of required moments (given that they can be achieved by the control surfaces at all). The resulting deflection commands $(\eta_L, \eta_R, \zeta)^T$ are sent to the actuators by the FCS. The response of the vehicle is measured and the control errors with respect to the commands $(\Delta\mu, \Delta\alpha, \Delta\beta)^T$ and the first derivatives $(\Delta\dot{\mu}, \Delta\dot{\alpha}, \Delta\dot{\beta})^T$ are calculated. These resulting deviations are input to three separate PID controllers which handle μ, α and β as independent domains, as described in Eqs. (16)– (18). Proportional gains k_P, integral gains k_I and differential gains k_D are

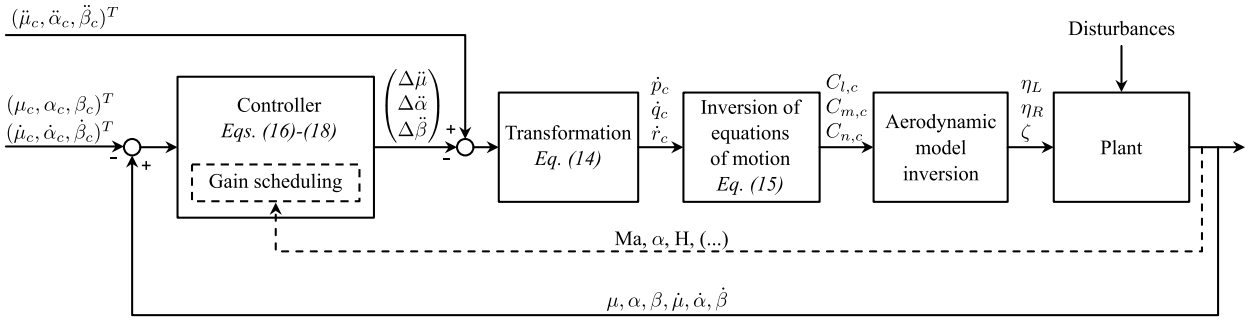

Fig. 6 Inner control loop architecture

used to process the control errors to additional acceleration terms $(\Delta\ddot{\mu}, \Delta\ddot{\alpha}, \Delta\ddot{\beta})^T$, which are subtracted from the guidance commands as feedback terms. The gains are determined by the flight controller via a gain scheduling based on the current flight condition (primarily the Mach number, angle of attack, and altitude). This combination of feedforward and feedback elements ensures a fast command response and good disturbance rejection. Figure 6 shows an overview of the architecture of the inner control loop.

$$\Delta\ddot{\mu} = k_{P,\ddot{\mu}} \underbrace{(\mu - \mu_c)}_{\Delta\mu} + k_{I,\ddot{\mu}} \int \Delta\mu \, dt + k_{D,\ddot{\mu}} \underbrace{(\dot{\mu} - \dot{\mu}_c)}_{\Delta\dot{\mu}}, \tag{16}$$

$$\Delta\ddot{\alpha} = k_{P,\ddot{\alpha}} \underbrace{(\alpha - \alpha_c)}_{\Delta\alpha} + k_{I,\ddot{\alpha}} \int \Delta\alpha \, dt + k_{D,\ddot{\alpha}} \underbrace{(\dot{\alpha} - \dot{\alpha}_c)}_{\Delta\dot{\alpha}}, \tag{17}$$

$$\Delta\ddot{\beta} = k_{P,\ddot{\beta}} \underbrace{(\beta - \beta_c)}_{\Delta\beta} + k_{I,\ddot{\beta}} \int \Delta\beta \, dt + k_{D,\ddot{\beta}} \underbrace{(\dot{\beta} - \dot{\beta}_c)}_{\Delta\dot{\beta}}. \tag{18}$$

Note that there is a somewhat hidden interdependency in the presented inversion approach which complicates its exact implementation: since the aerodynamic control surfaces not only affect the moments of the vehicle but also the total lift, drag, and side forces, they have a direct impact on $\dot{\gamma}$ and $\dot{\chi}$, which in turn affect the target rotational rates and accelerations according to Eqs. (8) and (14). Hence, in an exact implementation, a sole inversion of the aerodynamic model would not be sufficient, but instead, the required control surface deflections would need to be determined in an iterative loop with feedback of $\dot{\gamma}$ and $\dot{\chi}$. Such an iterative calculation will be very costly and might not be suitable for real-time applications. Fortunately in this case, the forces produced by the control surfaces are much smaller than the total forces acting on the vehicle itself, hence their effect on $\dot{\gamma}$ and $\dot{\chi}$ is very small. The implementation used for this paper therefore uses the current $\dot{\gamma}$ and $\dot{\chi}$ in every point of time, while the small errors produced by neglecting their dependency on the control surface deflections are compensated by the PID controllers.

All quantities required by the FCS will be measured or estimated by the hybrid navigation system (HNS), which provides the information directly to the FCS. A description of the HNS is found in [17], and details about the flight instrumentation are presented in [21]. In this paper, it is assumed that the measurements and estimations provided by the HNS are perfect, i.e., without any errors or delays. The effects of imperfect measurements on the performance of the proposed flight controller will be subject to future work. Under the discussed conditions, the controller only has to compensate for three sources of error: the actuator dynamics, the neglected effects of the aerodynamic control surfaces on $\dot{\gamma}$ and $\dot{\chi}$ discussed in the previous paragraph, and small numerical errors caused by the finite precision of the aerodynamic model inversion.

5 Closed-loop stability analysis

This section discusses the preliminary performance assessment of the controller concept introduced in Sect. 4. To evaluate the performance of the controller, the system dynamics of the open-loop and the closed-loop cases are compared at two different flight points which are representative examples of the planned trajectory of ReFEx. The specifics of both

Table 2 Flight points for closed-loop stability analysis

Parameter	Flight point	
	1	2
Mach number	4.0	0.8
Aerodynamic bank angle μ	180°	0°
Angle of attack α	−30°	6°
Angle of sideslip β	0°	0°
Altitude	23 km	8 km

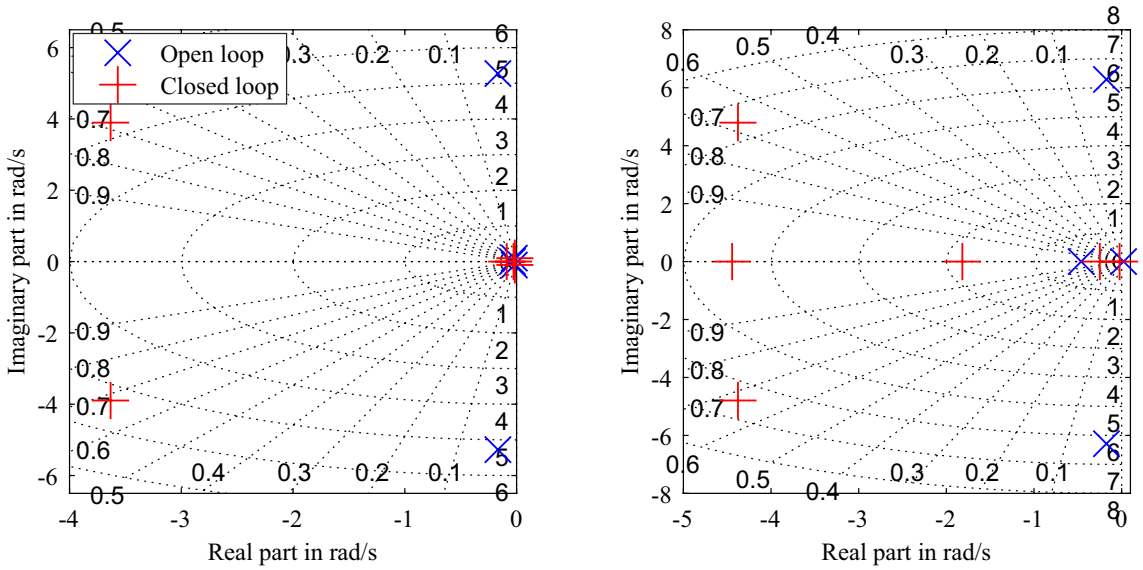

(a) Longitudinal motion **(b)** Lateral motion

Fig. 7 Flight point 1 (Mach 4, $\alpha = -30°$, $\mu = 180°$): eigenvalues of the longitudinal and lateral motion

flight points are found in Table 2. The feedback gains were tuned with the goal of improving the dynamic behavior of the vehicle regarding disturbance rejection and returning to the initial state, i.e., to achieve a higher damping and a slightly higher frequency of the dominant oscillatory modes while retaining a reasonable phase margin.

The linearization results presented here were obtained under the assumptions discussed in Sect. 3 (rigid-body dynamics, no actuator dynamics apart from deflection limits). The impact of these assumptions will be subject to future work.

5.1 Flight point 1: supersonic flight at negative angles of attack

A typical flight point for the supersonic re-entry phase of ReFEx is an inverted attitude flight at an angle of attack of −30° at Mach 4. The eigenvalues of the longitudinal and lateral motion of the vehicle (open loop and closed loop) at this flight point are shown in Fig. 7a and b, respectively. Analysis of the eigenvectors showed that the characteristic modes present in the longitudinal and lateral motion match the modes of typical commercial aircraft quite well. In the open-loop case, the short period mode is stable, but very lightly damped. The FCS improves the damping of the short period mode significantly. The slower poles near the origin are mostly energy based (comparable to the phugoid mode in typical aircraft) and include aperiodical components caused by the rate of altitude change and consequent change of dynamic pressure. These modes are very slow and marginally stable, but they are only of secondary interest for the flight controller as they have to be handled by the outer guidance loops. The closed-loop system also exhibits a stable aperiodical mode which corresponds to the integral term of $\Delta\alpha$ described in Eq. (17).

In the open-loop lateral motion, a fast and only slightly damped oscillation (corresponding to the Dutch roll mode typical for commercial aircraft) is observed which is significantly more damped in the closed-loop case (as expected). Two aperiodical modes are found in the open-loop system: first, the spiral, which is very slightly unstable but almost insignificant in the open-loop case, and second, the pure roll mode, which is faster and stable. The closed-loop system features four aperiodical modes: two correspond to the roll and spiral modes, which are now physically different because of the interfering flight controller, and the other two correspond to the integrator terms of $\Delta\mu$ and $\Delta\beta$ in Eqs. (16) and (18), respectively.

5.2 Flight point 2: subsonic flight at positive angles of attack

As can be seen in the stability envelope shown in Fig. 4, there is only a very narrow corridor (in terms of angles of attack) where ReFEx is sufficiently stable and controllable in transonic and low subsonic speed. As an exemplary point for this region, a subsonic condition at Mach 0.8 and 6° angle of attack in regular attitude ($\mu = 0°$) is chosen. The eigenvalues of the longitudinal and lateral motion at this flight point are shown in Figure 8a and b, respectively. The observed characteristic modes are comparable to those of commercial aircraft, as was the case for flight point 1.

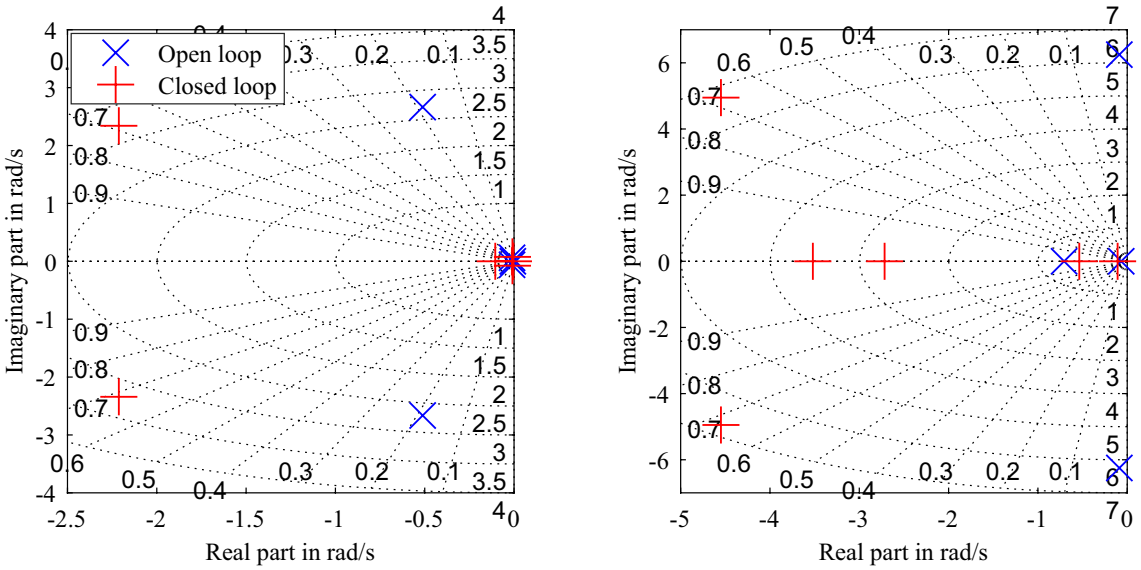

(a) Longitudinal motion **(b)** Lateral motion

Fig. 8 Flight point 2 (Mach 0.8, $\alpha = 6°$, $\mu = 0°$): eigenvalues of the longitudinal and lateral motion

In the open-loop case, the short period mode is slower and significantly better damped than it is in the supersonic open-loop case discussed previously (flight point 1). Closing the loop greatly increases the damping. The two slower eigenvalues are almost unaffected by the FCS, as was the case in flight point 1. The lateral motion shows a similar picture to flight point 1: the controller greatly damps the Dutch roll, which is stable but only lightly damped in the open-loop case. The spiral and roll modes are both stable in the open-loop system, but are further stabilized by the controller.

The lateral dynamics of both presented flight points are remarkably similar. This however is merely a coincidence, as multiple effects such as the dependency of the stability derivatives on the Mach number and the angle of attack as well as other effects, e.g., due to the different dynamic pressures appear to almost exactly cancel each other out.

It can be concluded that the closed-loop system is completely stable in both presented flight points under the discussed assumptions. The control authority of the aerodynamic control surfaces seems sufficient in these conditions, and consequently the controller can improve the vehicle's stability significantly along the foreseen trajectory. Since the stability analysis was performed assuming perfect actuators (no delays, no backlash, etc.), the stability and robustness of the controller in combination with realistic actuators has to be checked.

The results discussed above are to be understood as a preliminary proof of concept. In order to achieve a full proof of validity, the effects of latencies, erroneous sensor measurements, and actuator dynamics have to be investigated.

6 Time simulations

Time simulations were conducted for preliminary evaluation of the controller design and to validate the inversion of the aerodynamic model used for dynamic control allocation. Since the integration of the inner flight controller loops with the outer guidance loop is not finalized yet, the reference input commands $(\mu, \alpha, \beta)_c^T$ used for the simulation were taken from reference trajectories which are used for mission design and analysis. Details about their calculation are found in [15], and their usage in the design of the GNC algorithms is described in [17]. The model used for the time simulations and the stability analyses discussed in the previous sections is implemented in MATLAB/Simulink^{TM} and incorporates the nonlinear equations of motion in six degrees of freedom (6DoF) in a quaternion-based implementation, a World Geodetic System 1984 (WGS1984) geodetic model, and a model of the International Standard Atmosphere (ISA). The aerodynamic dataset used in the model is described in [14] and [22]. The simulations were performed assuming perfect (accurate and undelayed) measurements of the vehicle's position, attitude, velocity, etc. The actuators were modeled as second-order systems including limits for deflection angle, rate, and acceleration, but without any additional delays or backlash. The assumption of perfect measurements will of course not be applicable for robustness analysis and gain tuning, but it is valid for a preliminary evaluation of the controller concept.

The simulation presented here includes an example of the transition maneuver required to stay in a sufficiently

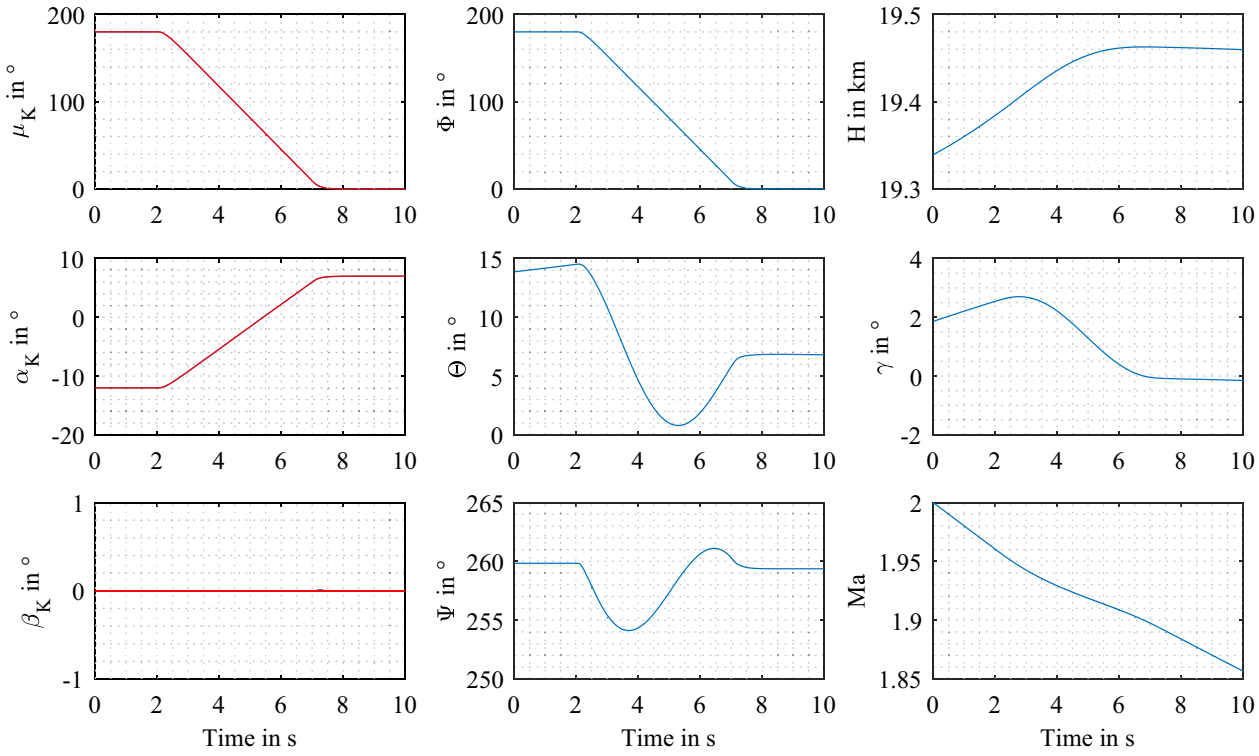

Fig. 9 Simulation results: aerodynamic angles, Euler angles, Mach number and altitude. Red: FCS commands, blue: vehicle response

stable flight corridor as discussed in Sect. 3. To restore a regular flight state from an inverted flight state, the vehicle transitions from $\mu = 180°$ and $\alpha = -12°$ to $\mu = 0°$ and $\alpha = 7°$ at Mach 2 and at an altitude of approximately 19 km. The initial conditions are derived from the aforementioned reference trajectories of ReFEx and hence correspond to a flight condition that will be encountered during the foreseen flight experiment. To perform this maneuver, a rolling motion around the velocity vector is necessary as well as a pitching motion around the body-fixed y-axis y_b. The maneuver is initiated 2 s after the simulation start and is defined in such a way that the required roll and pitch rotations of the vehicle w.r.t. the aerodynamic frame take place simultaneously within the maneuver time of 5 s, which requires a synchronized coordination of body-fixed roll, pitch, and yaw accelerations and rates as explained in Sect. 3.

The results of this simulation are shown in Figs. 9 and 10. The reference commands $(\mu, \alpha, \beta)_c^T$ to the FCS are shown in red, and the response of the vehicle is shown in blue. It is apparent that the controller manages to follow the commands very closely, e.g., the deviation in sideslip angle $\Delta\beta$ remains below 0.01° (the control errors $\Delta\mu$, $\Delta\alpha$ and $\Delta\beta$ are shown in Fig. 11). The small overshoots in μ and α at the initiation and termination of the rolling maneuver are caused by the actuator dynamics, as the actuators take a finite amount of time to reach the commanded deflection. When actuator dynamics are disabled in the simulation, the deviations are negligible and only caused by numerical inaccuracies, which shows that the controller successfully coordinates the roll, pitch and yaw accelerations and rates.

The maximum occurring absolute rudder deflection ζ is only about 7° and the canard deflections η_L and η_R are well below their maximum movable limits of ±15°, which implies that this combined transition maneuver could be executed in a shorter time if necessary.

It can be observed that, even though the roll accelerations $\dot{p}_K$ at the initiation and the termination of the maneuver are of the same absolute value, the corresponding asymmetric canard deflections are very different: at the initiation ($t = 2$ s), a positive yawing moment and a negative rolling moment are required. The yawing moment is almost exclusively produced by the rudder here, but its deflection also produces the desired rolling moment as a secondary effect, hence only a marginal difference between η_L and η_R is needed to achieve the total desired rolling moment. At the termination of the maneuver ($t = 7$ s), however, a positive rolling moment and a positive yawing moment are required. This time the negative rolling moment produced by the rudder is undesired and has to be compensated by the canards, hence the asymmetric canard deflection is significantly higher.

The absence of atmospheric disturbances and the assumption of perfect sensor measurements during the simulation

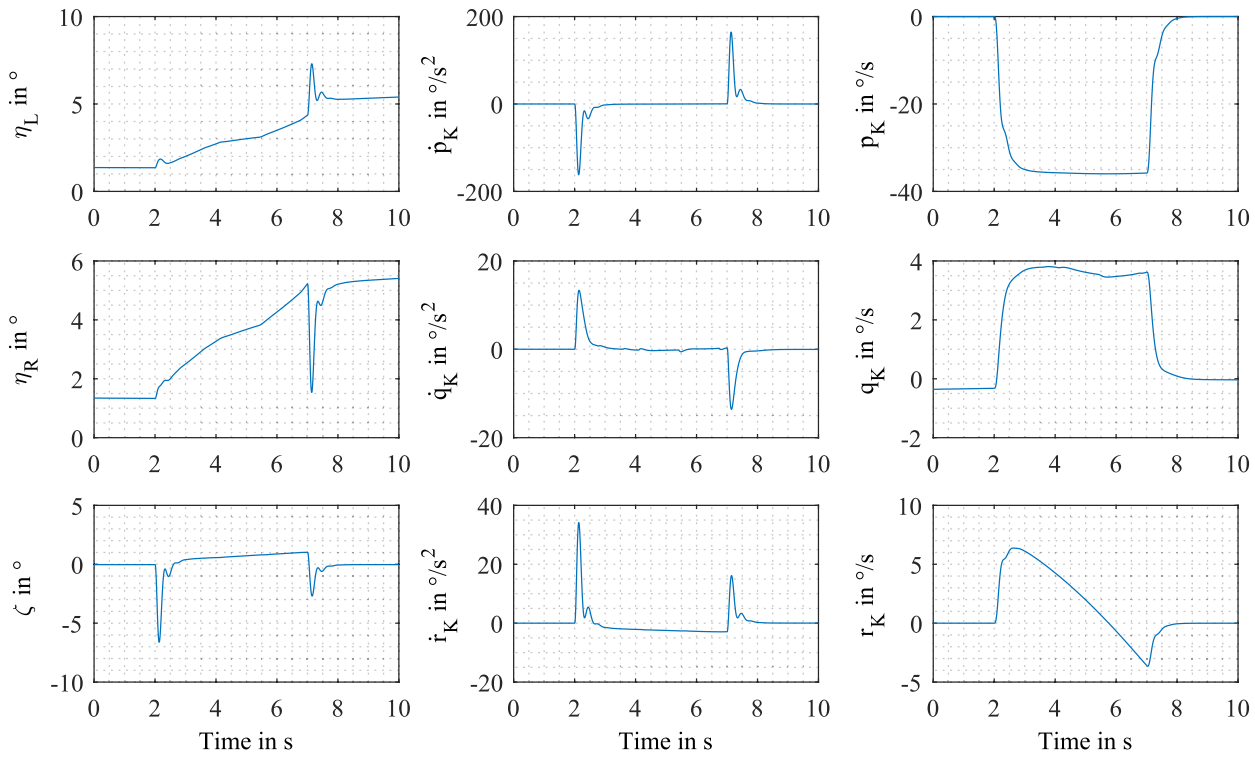

Fig. 10 Simulation results: control surface deflections, angular accelerations and rates

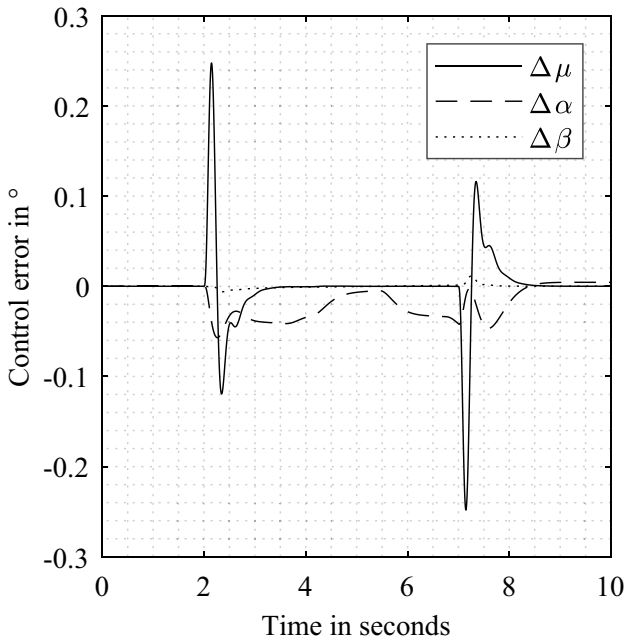

Fig. 11 Simulation results: control errors

certainly pose benevolent conditions for the flight controller, but the simulation results imply the validity of the controller concept introduced in Sect. 4.

7 Conclusions

The open-loop stability analysis discussed in Sect. 3 revealed that the flight envelope where the vehicle is sufficiently stable and controllable is existent, but relatively narrow. It was shown that a transition maneuver in the supersonic speed regime is necessary to stay within a sufficiently stable corridor.

In Sect. 4, a control concept was introduced, which includes feedforward elements (transformations to obtain the rotational accelerations and rates, inversion of the aerodynamic model) and feedback elements (PI controllers acting on the control error and its first derivative). The validity of the presented concept was discussed in Sect. 5, where the dynamics of the open-loop system were compared to the closed-loop system. It was found that the flight controller manages to stabilize the vehicle in the presented flight conditions. It is assumed that, given appropriate tuning of gains, the stability envelope of the closed-loop system will be very significantly larger than that of open-loop system, and that a controller can be found which stabilizes the vehicle in a sufficiently large flight corridor under realistic conditions to fulfill the mission.

The exemplary time simulation of a coordinated transition maneuver presented in Sect. 6 showed the capability of the controller to follow potentially demanding and combined

guidance commands (which were emulated by pre-defined reference commands) very closely, which implies the validity of the controller concept presented in Sect. 4, including the transformation from commands to rotational rates and accelerations and the inversion of the aerodynamic model.

8 Future work

Extensive closed-loop stability analysis including tuning of gains will be needed to further develop and fully validate the presented control concept. To achieve the final objective of proving the stability and robustness of the controller, these investigations will have to include the sensitivity of the controller

- to realistic atmospheric disturbances,
- to deviations in the atmospheric model,
- to measurement errors and delays of sensors,
- to imprecision and noise of estimated quantities,
- to actuator dynamics including delays and deflection inaccuracy,
- to deviations in mass, center of gravity and moments of inertia,
- to errors in the aerodynamic data.

This work is planned to be conducted mainly using exhaustive Monte Carlo simulations. Following this analysis, the introduced stability criteria based on the maximum real parts and the corresponding definition of the stability envelope can be refined, if necessary.

Furthermore, during investigation of the open-loop system dynamics, it was noticed that there are very significant downstream effects of the canards on the wings, sometimes resulting in large loss of lift on the wings. These effects can lead to roll control reversal in some flight conditions, since the increased lift at the canards can cause an even bigger loss of lift on the wings (and conversely, decreased lift at the canards may cause even bigger increase of lift at the wings), and hence the resulting roll of the vehicle can be opposite to the primary rolling moment of the canards. This aerodynamic effect can be compensated and accounted for by the flight controller, but the inversion of the aerodynamic model must be extremely precise, and hence the physical effects behind it must be very well studied and understood.

Acknowledgements Open Access funding provided by Projekt DEAL. The author would like to thank Mr. Wulf Mönnich from the DLR Institute of Flight Systems for his helpful advice in the field of flight dynamics and control and for his contributions to the development of the flight controller in the earlier phases of the project. Special thanks go to Dr. Nicolas Fezans, also from the DLR Institute of Flight Systems, for his guidance and counsel regarding the specifics of re-entry flight dynamics.

References

1. Wilken, J., Stappert, S., Bussler, L., Sippel, M., Dumont, E.: Future European Reusable Booster Stages: Evaluation of VTHL and VTVL Return Methods. In: 69th International Astronautical Congress, October 1–5, Bremen, Germany (2018)
2. Bussler, L., Wilken, J., Stappert, S., Sippel, M., Dietlein, I.M., Dumont, E.: Assessment of VTVL and VTHL Reusable First Stages. In: International Conference on High-Speed Vehicle Science Technology (HiSST), November 26–29, Moscow, Russia (2018)
3. Dumont, E., Ecker, T., Chavagnac, C., Witte, L., Windelberg, J., Klevanski, J., Giagkozoglou, S.: CALLISTO—Reusable VTVL Launcher First Stage Demonstrator. In: Space Propulsion Conference, May 14–18, Seville, Spain (2018)
4. Klevanski, J., Ecker, T., Riehmer, J., Reimann, B., Dumont, E., Chavagnac, C.: Aerodynamic Studies in Preparation for CALLISTO—Reusable VTVL Launcher First Stage Demonstrator. In: 69th International Astronautical Congress, October 1–5, Bremen, Germany (2018)
5. Rickmers, P., Bauer, W., Wübbels, G., Kottmeier, S.: ReFEx: Reusability Flight Experiment—A Project Overview. In: 8th European Conference for Aeronautics and Space Sciences (EUCASS), Conference on "Reusable Systems for Space Access" , July 1–4 , Madrid, Spain. EUCASS association (2019) https://doi.org/10.13009/EUCASS2019-584
6. Bauer, W., Rickmers, P., Kallenbach, A., Stappert, S., Wartemann, V., Merrem, C., Schwarz, R., Sagliano, M., Grundmann, J.T., Flock, A., Thiele, T., Kiehn, D., Bierig, A., Windelberg, J., Ksenik, E., Bruns, T., Ruhe, T., Elsäßer, H.: DLR Reusability Flight Experiment ReFEx. Acta Astronautica, vol. 168, pp. 57–68, Elsevier (2020). https://doi.org/10.1016/j.actaastro.2019.11.034
7. Rickmers, P., Bauer, W., Sippel, M., Stappert, S.: ReFEx: Reusability Flight Experiment—A Flight Experiment to Demonstrate Controlled Aerodynamic Flight from Hypersonic to Subsonic Velocities with a Winged RLV. In: 7th European Conference for Aeronautics and Space Sciences (EUCASS), July 3–6, Milan, Italy (2017) https://doi.org/10.13009/EUCASS2017-644
8. Eggers, Th.: The SHEFEX II Experimental Re-entry Vehicle—Presentation of Flight Test Results. In: 28th International Congress of the Aeronautical Science (ICAS), September 23–28, Brisbane, Australia (2012)
9. Lorenz, S., Bierig, A.: Robustness Analysis Related to the Control Design of the SHEFEX-II Hypersonic Canard Control Experiment. In: AIAA Guidance, Navigation, and

Control Conference, August 19–22, Boston. Massachusetts, USA (2013). https://doi.org/10.2514/6.2013-4857
10. Snell, S.A., Enns, D.F., Garrard, W.L.: Nonlinear inversion flight control for a supermaneuverable aircraft. AIAA J. Guidance Control Dyn. (1992). https://doi.org/10.2514/3.20932
11. da Costa, R.R., Chu, Q.P., Mulder, J.A.: Reentry flight controller design using nonlinear dynamic inversion. AIAA J. Spacecr. Rockets (2003). https://doi.org/10.2514/2.3916
12. Juliana, S., Chu, Q.P., Mulder, J.A., van Baten, T.J.: Flight Control of Atmospheric Re-entry Vehicle with Non-linear Dynamic Inversion. In: AIAA Guidance, Navigation, and Control Conference, August 16–19, Providence. Rhode Island (2004). https://doi.org/10.2514/6.2004-5330
13. Kirchhartz, R., Schmidt, A., Hörschgen-Eggers, M., Kallenbach, A.: ReFEx Launch With a Sounding rocket—a Challenging Mission on a Reliable Carrier. In: 8th European Conference for Aeronautics and Space Sciences (EUCASS), Conference on "Reusable Systems for Space Access", July 1–4, Madrid, Spain. EUCASS association (2019) https://doi.org/10.13009/EUCASS2019-480
14. Merrem, C., Wartemann, V., Eggers, T.: Preliminary Aerodynamic Design of a Reusable Booster Flight Experiment. In: International Conference on High-Speed Vehicle Science Technology (HiSST), November 26–29, Moscow, Russia (2018)
15. Stappert, S., Rickmers, P., Bauer, W., Sippel, M.: Mission Analysis and Preliminary Re-entry Trajectory Design of the DLR Reusability Flight Experiment ReFEx. In: 8th European Conference for Aeronautics and Space Sciences (EUCASS), Conference on "Reusable Systems for Space Access", July 1–4, Madrid, Spain. EUCASS association (2019) https://doi.org/10.13009/EUCASS2019-436
16. Bauer, W., Rickmers, P., Kallenbach, A., Stappert, S., Schwarz, R., Sagliano, M., Häseker, J.S., Flock, A., Thiele, T., Bierig, A., Windelberg, J., Ksenik, E.: Upcoming DLR Reusability Flight Experiment. In: 68th International Astronautical Congress, September 25–29, Adelaide, Australia (2017)
17. Schwarz, R., Kiehn, D., Trigo, G.F., Razgus, B., Wenzel, A., Seelbinder, D., Sommer, J., Theil, S., Markgraf, M., Dumke, M., Reigenborn, M., Bestard Körner, M., Solari, M., Braun, B., Pfau, D.: Overview of Flight Guidance, Navigation, and Control for the DLR Reusability Flight Experiment (ReFEX). In: 8th European Conference for Aeronautics and Space Sciences (EUCASS), Conference on "Reusable Systems for Space Access", July 1–4, Madrid, Spain. EUCASS association (2019) https://doi.org/10.13009/EUCASS2019-739
18. Etkin, B., Reid, L.D.: Dynamics of Flight: Stability and Control, Third edn. Wiley, Hoboken (1996)
19. Sagliano, M., Trigo, G.F., Schwarz, R.: Preliminary Guidance and Navigation Design for the Upcoming DLR Reusability Flight Experiment (ReFEx). In: 69th International Astronautical Congress, Bremen, Germany
20. Fezans, N., Alazard, D., Imbert, N., Carpentier, B.: Robust LPV control design for a RLV during reentry. In: AIAA Guidance, Navigation, and Control Conference, August 2–5, Toronto. Ontario, Canada (2010). https://doi.org/10.2514/6.2010-8194
21. Thiele, T. and Siebe, F. and Flock, A. and Gülhan, A.: Flight Instrumentation for the Reusability Flight Experiment ReFEx. In: 8th European Conference for Aeronautics and Space Sciences (EUCASS), Conference on "Reusable Systems for Space Access", July 1–4, Madrid, Spain. EUCASS association (2019) https://doi.org/10.13009/EUCASS2019-690
22. Merrem, C., Kiehn, D., Wartemann, V., Eggers, T.: Aerodynamic Design of a Reusable Booster Stage Flight Experiment. 8th European Conference for Aeronautics and Space Sciences (EUCASS), Conference on "Reusable Systems for Space Access", July 1-4, Madrid, Spain. EUCASS association (2019) https://doi.org/10.13009/EUCASS2019-644